Electron cyclotron current drive simulations for finite collisionality plasmas in Wendelstein 7-X using the full linearized collision model

Gernot Kapper,[1, a)] Sergei V. Kasilov,[1, 2] Winfried Kernbichler,[1] Andreas F. Martitsch,[1] Martin F. Heyn,[1] Nikolai B. Marushchenko,[3] and Yuriy Turkin[3]

[1)] *Fusion@ÖAW, Institut für Theoretische Physik - Computational Physics, Technische Universität Graz, Petersgasse 16, A–8010 Graz, Austria*

[2)] *Institute of Plasma Physics, National Science Center "Kharkov Institute of Physics and Technology", ul. Akademicheskaya 1, 61108 Kharkov, Ukraine*

[3)] *Max-Planck-Institut für Plasmaphysik, Wendelsteinstr. 1, D-17491 Greifswald, Germany*

(Dated: 26 August 2016)

The Electron Cyclotron Current Drive (ECCD) efficiency is usually modeled in collisionless limits. While such models are sufficient for plasmas with rather low collisionality, they might underestimate the current drive in plasmas at low temperatures as they occur at an initial phase of device operation. In this paper, the impact of finite collisionality effects on the wave-induced current drive is studied for a high-mirror configuration of Wendelstein 7-X using a combination of the drift kinetic equation solver NEO-2 and the ray-tracing code TRAVIS for a realistic set of plasma parameter profiles. The generalized Spitzer function, which describes the ECCD efficiency in phase space, is modeled with help of NEO-2, which uses the full linearized Coulomb collision operator including energy and momentum conservation. Within this approach the linearized drift kinetic equation is solved by means of the field line integration technique without any simplifications on device geometry. Results of the ray-tracing code TRAVIS using the ECCD efficiency from NEO-2 within the adjoint approach show a significant difference of the driven current as compared to commonly used collisionless models for the ordinary as well as the extraordinary second harmonic mode.

[a)] gernot.kapper@tugraz.at

I. INTRODUCTION

In the Wendelstein 7-X stellarator[1] low-order rational flux surfaces are avoided in the plasma core by its low-shear concept since these can cause the formation of magnetic islands. In turn, such resonant flux surfaces are placed at the plasma edge forming an island divertor configuration. These special device characteristics can be destroyed by a small bootstrap current which has to be compensated by Electron Cyclotron Current Drive (ECCD)[2], where the resonant interaction of electrons and incident radio-frequency-waves drives a parallel current[3]. The Electron Cyclotron Resonance Heating (ECRH) system of the Wendelstein 7-X stellarator is designed for ten gyrotrons each with a power up to 1 MW at a wave frequency of 140 GHz at continues operation[4]. The two main ECRH/ECCD scenarii are heating and current drive with the X2-mode for low and moderate densities and the O2-mode for high densities, which are both investigated in this paper.

The efficiency of current drive by microwave injection, defined by the generalized Spitzer function using the adjoint approach[5], is well studied in asymptotical collisionality limits, namely for the collisionless case where the 2D bounce averaged equation is solved and in the high collisionality limit where the classical Spitzer function[6] for homogenous magnetic fields can be applied. In contrast to the collisionless limit, for finite collisionality, the generalized Spitzer function has a finite value in the trapped region[7] (but smaller than in the high collisionality limit) and also has an offset in the passing region[8]. These features can qualitatively be reproduced by interpolation between asymptotical limits[9]. However, direct calculations of the generalized Spitzer function in the case of finite collisionality exhibits also a feature which can not be expected from such an interpolation. This feature is due to the symmetric part of this function with respect to parallel velocity, which is absent in asymptotical limits, resulting from the combined action of the magnetic mirroring and of the collisions. This part, which is localized around the trapped-passing boundary in the long mean free path regime, is also responsible for the bootstrap effect. As shown analytically in Ref. 10 and demonstrated later numerically in Refs. 11–13, this symmetric part of the generalized Spitzer function can be used for current drive by waves with symmetric spectra in the parallel wave number. Here, the generalized Spitzer function, which is the normalized distribution function of the parallel flow, is calculated by the neoclassical drift kinetic equation solver NEO-2[14], which treats plasmas with finite collisionality without any

simplification on device geometry by means of the field line integration technique[15]. In this code the kinetic equation is solved using the full linearized Coulomb collision operator including energy and momentum conservation[16]. Originally, NEO-2 was developed for the computation of mono-energetic neoclassical transport coefficients in stellarators[17] and for the computation of the distribution functions in tokamaks[11]. However, recent progress such as the development of a quasilinear version for non-axisymmetric tokamaks[18] as well as ongoing technical improvements such as parallelization for a more efficient computation of the generalized Spitzer function in stellarators[12,13] resulted in a more general version of the code.

In this paper the impact of finite collisionality on ECCD is studied with the ray-tracing code TRAVIS[19] using the local current drive efficiency in the non-relativistic limit without simplifications to the collisional model computed by NEO-2. The structure of this paper is as follows, in Sec. II the derivation of the parallel driven current density within the adjoint approach is presented, in Sec. III results of the current drive efficiency computed by NEO-2 as well as results from ray-tracing are presented for realistic plasma parameter profiles from an initial stage of device operation in Wendelstein 7-X, while in Sec. IV a conclusion of the observed effects is given.

II. CURRENT DRIVE USING THE ADJOINT APPROACH

A. Conductivity problem

Following Ref. 14, the linearized drift kinetic equation ignoring cross-field drift for the current drive problem is given as,

$$\hat{L}_0 f_\mathrm{M} g_3 = q_3 f_\mathrm{M}, \tag{1}$$

where f_M is a local Maxwellian, g_3 is the distribution function driven by the parallel electric field, $q_3 = v_\parallel B$ is the source term for the conductivity problem, B is the magnetic field module, $v_\parallel$ is the parallel velocity module, and $\hat{L}_0$ is an integro-differential operator defined as,

$$\hat{L}_0 = v\lambda h^\vartheta \frac{\partial}{\partial \vartheta} - \hat{L}_C, \tag{2}$$

where v is the particle velocity module, $\lambda = v_\parallel / v = \lambda(\vartheta, \eta)$ is the pitch parameter, h^ϑ is the contra-variant poloidal component of the unit vector along the magnetic field line, ϑ is a

field line parameter, and $\hat{L}_C$ is the full linearized Coulomb collision integral including energy and momentum conservation. Operator (2) is written in terms of integrals of motion v and normalized perpendicular adiabatic invariant $\eta = v_\perp^2/(v^2 B)$ which are conserved in zero order over the Larmor radius. Here, the cross-field rotation term was neglected because it has a small effect on this distribution function in finite collisionality regimes as well as at low collisionalities where the electrons are mostly in the $1/\nu$ regime. Besides Eq. (1), function g_3 must satisfy two additional constraints which remove the null-space of this equation[14],

$$\left\langle \int \mathrm{d}^3 v \; f_\mathrm{M} g_3 \right\rangle = \left\langle \int \mathrm{d}^3 v \; v^2 f_\mathrm{M} g_3 \right\rangle = 0. \tag{3}$$

Eq. (1) is solved on a long enough field line, $0 < \vartheta < 2\pi\iota N_t$, where ι is the rotational transform and $N_t \gg 1$ is a number of toroidal periods large enough to cover the magnetic flux surface in a way allowing for a sufficiently accurate interpolation. The distribution function g_3 is related to the generalized Spitzer function g_sp, which is independent of collisionality in asymptotical limits, as follows,

$$g_\mathrm{sp} = \frac{1}{l_C B_\mathrm{ref}} g_3, \qquad l_C = \frac{T_e^2}{\pi n_e e^4 \ln \Lambda_{ee}}, \tag{4}$$

where l_C is the mean free path, B_ref is a reference magnetic field module, T_e is the electron temperature, n_e is the electron density, e is the electron charge, and $\ln \Lambda_{ee}$ is the Coulomb logarithm as defined in Ref. 20. The thermodynamic flux connected to the current drive problem is defined as,

$$I_3 = n_e \left\langle V_{\parallel e} B \right\rangle = - \left\langle \int d^3 v q_3^\dagger \delta f_\mathrm{RF} \right\rangle, \tag{5}$$

where $V_{\parallel e}$ is the electron parallel flow velocity, $< \ldots >$ denotes neoclassical flux surface average (average over the volume between neighboring flux surfaces), the cross denotes an opposite parallel velocity sign, and the distribution function δf_RF is the solution to the linear current drive problem,

$$\hat{L}_0 \delta f_\mathrm{RF} = Q_\mathrm{RF}, \tag{6}$$

where

$$Q_\mathrm{RF} = \hat{L}_\mathrm{QL} f_\mathrm{M} = -\frac{1}{J} \frac{\partial}{\partial v^i} \left(J \Gamma^i_\mathrm{RF} \right) \tag{7}$$

is a quasilinear particle source in phase space due to the resonant interaction with radio-frequency-waves, Γ^i_RF is the wave-induced quasilinear diffusion flux density, and $\hat{L}_\mathrm{QL}$ is a

quasilinear diffusion operator acting on the local Maxwellian f_{M}. Here, a co- and contravariant notation with respect to the velocity space components v^i is used, and J is a phase space Jacobian.

Using the same adjoint approach as in Ref. 5, the averaged parallel electron current density $j_{\parallel e}$ can be expressed as follows,

$$\begin{aligned}\left\langle j_{\parallel e}B\right\rangle &= -e\left\langle \int d^3v q_3^\dagger \delta f_{\mathrm{RF}}\right\rangle \\ &= -e\left\langle \int d^3v \delta f_{\mathrm{RF}} f_{\mathrm{M}}^{-1}(q_3^\dagger f_{\mathrm{M}})\right\rangle \\ &= -e\left\langle \int d^3v \delta f_{\mathrm{RF}} f_{\mathrm{M}}^{-1}(\hat{L}_0^\dagger f_{\mathrm{M}} g_3^\dagger)\right\rangle \\ &= -e\left\langle \int d^3v g_3^\dagger \hat{L}_0 \delta f_{\mathrm{RF}}\right\rangle, \end{aligned} \tag{8}$$

where $\hat{L}_0^\dagger f_{\mathrm{M}} g_3^\dagger = q_3^\dagger f_{\mathrm{M}}$ and the adjointness relation,

$$\left\langle \int d^3v G\hat{L}_0 f_{\mathrm{M}} F\right\rangle = \left\langle \int d^3v F\hat{L}_0^\dagger f_{\mathrm{M}} G\right\rangle, \tag{9}$$

is used. Finally, the parallel current density can be directly linked to the source term in Eq. (6),

$$\left\langle j_{\parallel e}B\right\rangle = -el_C B_{\mathrm{ref}}\left\langle \int d^3v g_{\mathrm{sp}}^\dagger Q_{\mathrm{RF}}\right\rangle = el_C B_{\mathrm{ref}}\left\langle \int d^3v \frac{\partial g_{\mathrm{sp}}^\dagger}{\partial v^i}\,\Gamma_{\mathrm{RF}}^i\right\rangle, \tag{10}$$

where the adjoint generalized Spitzer function is expressed through the generalized Spitzer function (4) as follows, $g_{\mathrm{sp}}^\dagger(v_\parallel) = g_{\mathrm{sp}}(-v_\parallel)$.

B. Distribution function for full linearized collision model

The velocity dependence of the NEO-2 solution to integro-differential equation (1) pertinent to the full linearized collision model is expanded over a complete set of test functions $\varphi_m(v)$,

$$g_3^\sigma(\vartheta, v, \lambda) = \sum_{m=0}^{M} g_{3,m}^\sigma(\vartheta, \eta(\vartheta,\lambda))\varphi_m(v), \tag{11}$$

where $M+1$ is the number of basis functions, and σ is the parallel velocity sign. The expansion coefficients $g_{3,m}^\sigma(\vartheta,\eta)$ of the generalized Spitzer function are computed by NEO-2 using a conservative 2D finite difference scheme of third order over the normalized perpendicular adiabatic invariant η and of the first order over the field line parameter ϑ with an adaptively

refined η-grid in order to resolve all trapped-passing boundary layers[14]. In previous versions of NEO-2, the basis functions $\varphi_m(v)$ were fixed to be generalized Laguerre polynomials of order 3/2 (Sonine polynomials). This choice was not an intrinsic limitation of the code and has been overcome recently allowing the usage of an arbitrary complete set of basis functions, which are not necessarily orthogonal. For the computation of flux surface averaged neoclassical diffusion coefficients, a typical number of basis functions used is between $M = 3$ and $M = 5$. Further increase of the number of Sonine polynomials results in an expansion of the solution by high order polynomials which tend to diverge at higher velocities. However, for the computation of the distribution function for ECCD applications a stable computation up to $v = 5v_{th}$ is of interest, which is computationally a rather difficult task when using a polynomial basis. In contrast to Sonine polynomials, which are globally defined on the whole velocity space, the usage of local basis functions, such as basis splines[21], allow to increase the upper velocity limit and the velocity resolution using the same number of basis functions as with the Sonine basis.

For the computations of the generalized Spitzer function, cubic basis splines are used resulting in a velocity dependence of the solution represented by piecewise cubic polynomials. Another application of NEO-2 such as the investigation of NTV in non-axisymmetric tokamaks[18] make it necessary to use low order basis splines, e.g., first order splines (hat functions), in order to resolve resonances accurately. These approaches and the pertinent numerical schemes are presented in detail in Ref. 14. The derivation of the matrix elements of the full linearized Coulomb collision operator including extensive benchmarks of various sets of basis functions will also be presented in an upcoming separate publication.

C. Computational treatment

1. Data precomputation

The high dimensionality of the problem, which is 5D for a given magnetic configuration with fixed plasma parameter profiles in case of a stellarator, makes the precomputation of the generalized Spitzer function inevitable. Therefore, the local NEO-2 solutions are precomputed on a prescribed set of flux surfaces, where on each flux surface the drift kinetic equation is solved along a single field line. The number of traced toroidal field periods N_t

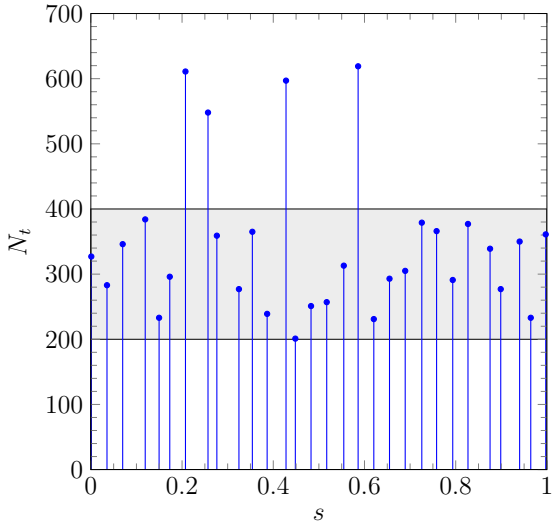

FIG. 1. Total number of toroidal field periods N_t as a function of the normalized toroidal flux s. The gray band indicates the intended lower and upper limits, respectively, for precomputation.

until the field line is closed artificially, defines the poloidal accuracy of the reconstruction process of the distribution function. The prescribed set of flux surfaces is chosen in a way that N_t per flux surface is within a defined boundary between 200 and 400 periods. The lower boundary guarantees an accurate computation, whereas the upper boundary keeps memory and runtime treatable. In a first step, these flux surfaces are uniformly distributed in the normalized toroidal flux s and are, if necessary, shifted from its initial distribution to avoid computation close to low-order rational flux surfaces. This is important to avoid a closure of the field line after only a few toroidal periods, which would result in poor poloidal resolution and as a consequence in extremely low accuracy of the flux surface averages. As seen from Fig. 1, the restriction to an intended number of periods is not possible with a purely uniform distribution due to resonances, therefore, the distribution is adaptively modified. Since the restriction can not be fulfilled everywhere without significantly violating the initial uniform distribution, a slightly larger number of periods is accepted for some values of s. The resulting set of flux surfaces and pertinent collisionality parameters computed from plasma parameter profiles is used as input for one NEO-2 run per flux surface.

In NEO-2 the field line is separated into domains which can be solved independent of each other. This allows an efficient parallelization of the code with almost ideal speedup with the number of computing nodes. Despite that NEO-2 is an efficient solver in sense of runtime and memory demands as shown in Ref. 14, the usage of the full linearized Coulomb collision

operator expanding the velocity dependence of the solution with several basis functions and rather long field lines, would not be treatable with reasonable effort without code parallelization. The computed solution on a dense mesh in phase space leads to rather large amounts of data ($\sim$ 100 GB per configuration and pertinent profile) stored in the HDF5 data format[22]. Since these data should be used as input also for other applications, the focus was on the development of an interface allowing straightforward access to the precomputed results.

2. Data access

The generalized Spitzer function acting as a current drive efficiency in phase space has to be evaluated along the microwave beam propagating through the plasma. Therefore, it has to be known for any point $(\mathbf{x}, v, \lambda)$ in phase space, where $\mathbf{x} = (s, \vartheta_b, \varphi_b)$ are Boozer coordinates being the normalized toroidal flux, poloidal and toroidal angles, respectively. From the local solution of the linear current drive problem $g_3^\sigma(\vartheta, v, \lambda)$, the solution to the 5D problem is reconstructed by linear interpolation over the radial coordinate and over the periodic Boozer angles. These periodic Boozer angles are related to the field line parameter ϑ via the relations,

$$\vartheta_b = \vartheta_0 + \vartheta, \qquad \varphi_b = \varphi_0 + \frac{\vartheta - \vartheta_0}{\iota}, \tag{12}$$

where ϑ_0 and φ_0 are the starting points of the field line and ι is the rotational transform. The values of ϑ, where the drift kinetic equation is solved, are adaptively distributed by the solver. Transformations of the field line parameter to Boozer coordinates as given in Eq. (12) results in Fig. 2, where a zoomed depiction of points where the problem is actually solved is given. It should be noted that the depiction of a whole flux surface with $0 < \vartheta_b < 2\pi$ and $0 < \varphi_b < 2\pi/N$ ($N = 5$ for Wendelstein 7-X) would result in a grid which size can be estimated with $N_t \times N_{\varphi_b}$, where typical values are $N_t = 400$ and $N_{\varphi_b} = 600$. In the center of the figure an arbitrary point of interest is marked by a cross in order to indicate the used points of precomputed values for linear interpolation. First, interpolation along two segments on the same field line enclosing the point is performed, while in a second step interpolation is done in the poloidal direction apart from the field line. Since the point of interest will usually be located between two precomputed flux surfaces, this procedure is performed on two flux surfaces enclosing the point with subsequent radial interpolation.

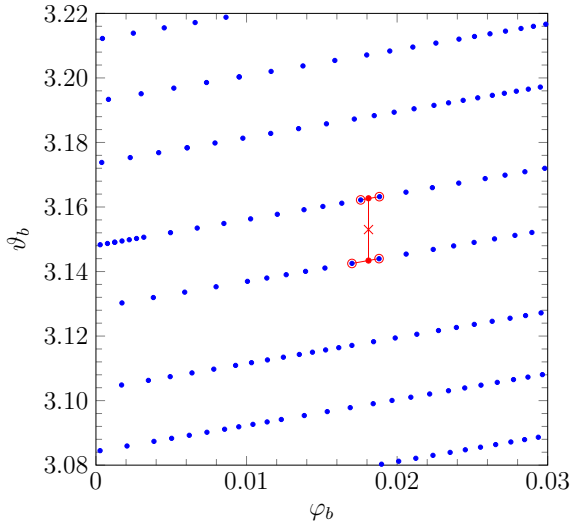

FIG. 2. Depiction of precomputed data points (•) by NEO-2 on a single flux surface. An arbitrary point of interest (×) is shown, where the required data points for interpolation are highlighted (○). The non-equal spacing of the data points is a consequence of the adaptive level placement in NEO-2 as shown in Ref. 14.

As a consequence, one spatial point requires eight precomputed values of NEO-2. The use of linear interpolation is justified by the dense grid in the periodic Boozer angles and the similarity of neighboring flux surfaces.

In order to find the relevant precomputed data points to a requested point on the 3D $(s, \vartheta_b, \varphi_b)$-grid, fast lookup routines based on binary search were implemented. The coefficients to reconstruct the distribution function, $g^{\sigma}_{3,m}(\vartheta, \eta(\vartheta, \lambda))$, are read from the data base using special features of the HDF5 library where only portions of a dataset (so-called hyperslabs[22]) are read in order to reduce disk operations. In addition, in order to speedup consecutive calls of the interface, all required information for interpolation of the previous spatial point is cached as long as the spatial position does not change. The time for querying one spatial point is of the order of milliseconds, while the evaluation of several velocities takes almost no extra time due to the described data caching. Therefore, the usage of the NEO-2 interface does not significantly harm the interactive usage of TRAVIS.

III. RESULTS

A. Current drive efficiency with NEO-2

The impact of finite plasma collisionality on ECCD is investigated using plasma parameter profiles from the transport code NTSS[23] and a high-mirror configuration of Wendelstein 7-X computed by the equilibrium code VMEC[24] as depicted in Figs. 3 and 4. The plasma parameters correspond to a collisionality at the onset of the long mean free path regime, where the collisionality is roughly three times smaller than needed for the plateau regime. Therefore, this profile represents an initial stage of device operation, where finite collisionality effects play a more significant role than at higher temperatures.

Heating by rf-waves is mainly performed close to the field maximum where the absorption of the wave energy by passing particles usually dominates the amount of energy absorbed by trapped particles. Therefore, the behavior of the generalized Spitzer function at spatial points around the field maximum is of special interest and is investigated in the following. The magnetic field module at half radius is given in Fig. 4, where some spatial points of interest are marked. Results of the generalized Spitzer function from NEO-2 for finite collisionality pertinent to given plasma parameters together with results for the long mean free path regime from the code SYNCH[25] for two different particle velocities, $v = v_T$ and $v = 3v_T$, are presented in Fig. 5. Here, $v_T = \sqrt{2T_e/m_e}$ is the thermal velocity, where T_e and m_e are electron temperature and electron mass, respectively. SYNCH is a fully relativistic code for the computation of the generalized Spitzer function in the long mean free path regime for general toroidal geometry and all types of flux coordinates. Both, the internal TRAVIS model, where the generalized Spitzer function is approximated in the collisionless limit, and the SYNCH model conserve parallel momentum. It has been shown that the high speed limit models can significantly underestimate the current drive efficiency in contrast to collisionless models with parallel momentum conservation[26].

It can be seen that the generalized Spitzer function with finite collisionality effects taken into account is strictly antisymmetric only at the absolute field maximum, and nearly antisymmetric for points in the bean-shaped plane $\varphi_b = 0$ in which the absolute maximum is located. For regions apart from the field maximum in toroidal directions, a significant symmetric part arises in the trapped region which can be explained by a combined effect of

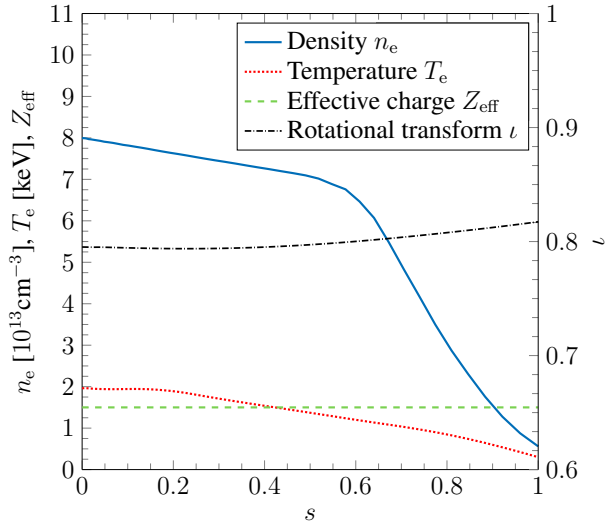

FIG. 3. Plasma parameter profiles computed by the transport code NTSS[23] and the rotational transform ι as functions of the normalized toroidal flux s.

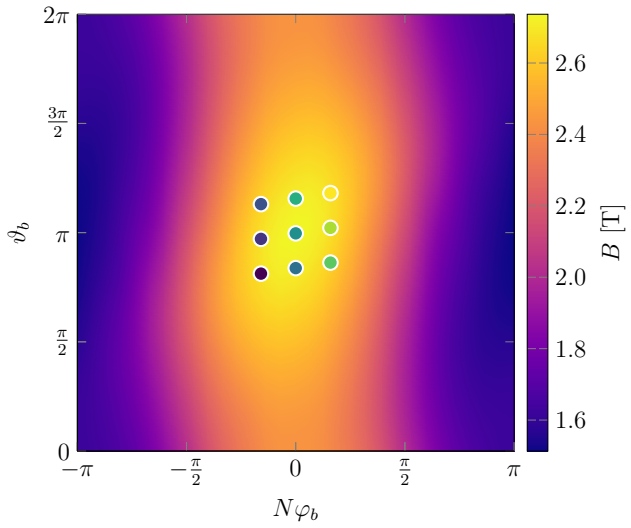

FIG. 4. Magnetic field module at flux surface $s = 0.25$ as function of Boozer angles ($N = 5$ for Wendelstein 7-X).

mirroring force and trapping/detrapping due to collisions. While finite collisionality leads to an offset also in the passing domain of the distribution function, the symmetric part is also of special interest because it is responsible for current drive by waves with symmetric spectra[10]. These effects become smaller at higher particle velocities where the distribution function converges to the collisionless limit.

In order to further investigate the symmetric part of the generalized Spitzer function,

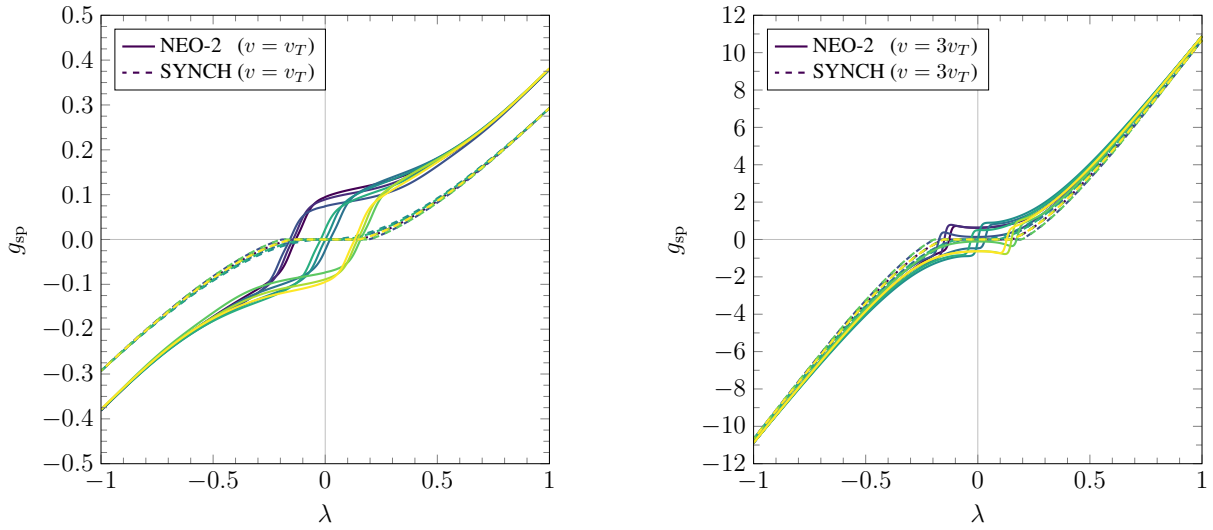

FIG. 5. Generalized Spitzer function for finite collisionality computed by NEO-2 (solid) and for the collisionless limit computed by SYNCH (dashed) as a function of the pitch parameter $\lambda = v_\parallel/v$. Line colors correspond to respective marker colors in Fig. 4.

this function is integrated over the pitch parameter in the trapped domain,

$$\overline{g_{\mathrm{sp}}^{(\mathrm{tr})}}(\vartheta, x) = \int\limits_{-\lambda_{\mathrm{tp}}(\vartheta)}^{+\lambda_{\mathrm{tp}}(\vartheta)} d\lambda g_{\mathrm{sp}}(\vartheta, \lambda(\eta, \sigma), x), \tag{13}$$

with

$$\lambda_{\mathrm{tp}}(\vartheta) = \sqrt{1 - \frac{B(\vartheta)}{B_{\mathrm{max}}}}, \tag{14}$$

where B_{max} is the maximum magnetic field module on the flux surface. The distribution of the resulting scalar (13) over the angles (this quantity is identical zero in asymptotical limits) is shown in Fig. 6 for two velocity values, $v = v_T$ and $v = 3v_T$, respectively. This dependence is partly similar to Ref. 8 where the angular distribution of the mono-energetic distribution function for $\lambda = 0$ has been studied.

From Fig. 5 it is expected that the sign of the mean value of the generalized Spitzer function in the trapped domain is mainly determined by the toroidal Boozer angle. However, as seen from Fig. 6 this is only the case in the vicinity of the absolute field maximum. At toroidal positions apart from the bean-shaped poloidal plane, the sign is determined mainly by the poloidal Boozer angle what is similar to the up-down-asymmetry in tokamaks[11]. Summarizing, the non-vanishing mean values of the trapped region of the generalized Spitzer

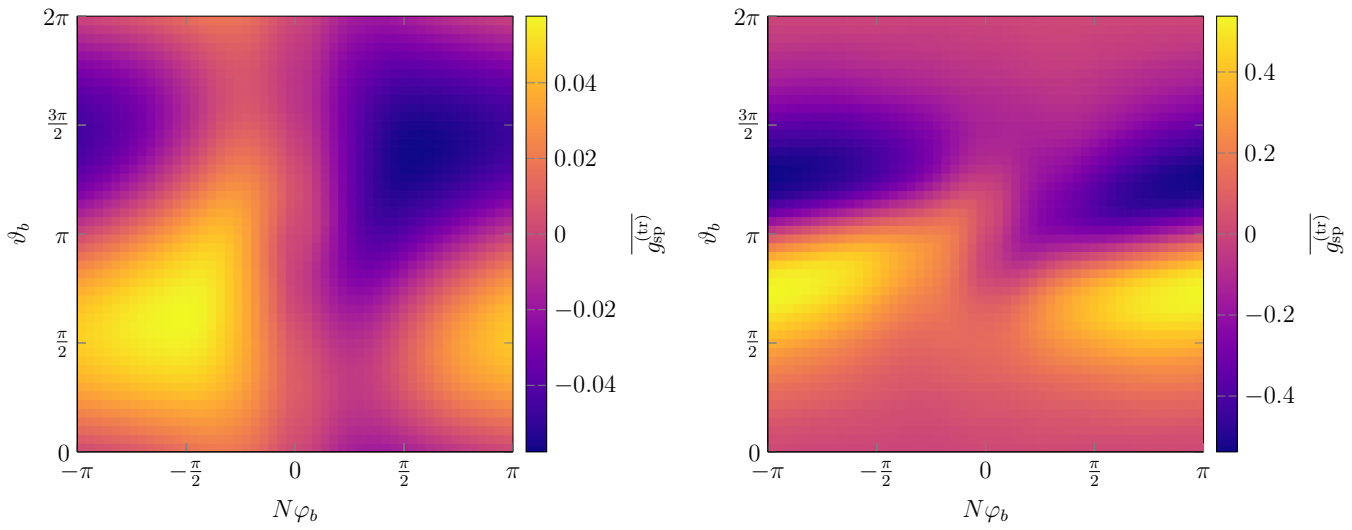

FIG. 6. Pitch-angle integral in the trapped domain of the generalized Spitzer function (13) for velocity values $v = v_T$ (left) and $v = 3v_T$ (right) as functions of Boozer angles on flux surface $s = 0.25$.

function on almost the whole flux surface indicate significant symmetric parts of this function which would not be seen by collisionless models.

B. ECCD computations within a ray-tracing procedure

In TRAVIS the geometrical optics approach is used for the computation of ECCD, where the quasilinear flux density Γ^i_{RF} of Eq. (7) is described in a local approximation, i.e., it differs from zero in velocity space only at the resonance line where the (multiple) cyclotron resonance condition taking into account Doppler shift is fulfilled,

$$\omega = n\omega_c + k_\parallel v_\parallel. \tag{15}$$

Here, ω is the wave frequency, n is the cyclotron harmonic index, $\omega_c = \omega_{c0}/\gamma$ is the relativistic electron cyclotron frequency, $\gamma = (1 - v^2/c^2)^{-1/2}$ is the relativistic factor, and $k_\parallel$ is the parallel wave vector with respect to the magnetic field. In this approach the wave-induced quasilinear diffusion flux density (7) is given as follows,

$$\Gamma^i_{\mathrm{RF}} = -\delta(\omega - n\omega_c - k_\parallel v_\parallel) D_0^{ij} \frac{\partial f_M}{\partial v^j}, \tag{16}$$

where D_0^{ij} are quasilinear diffusion coefficients. Then, Eq. (10) takes the form

$$\left\langle j_\parallel B \right\rangle = -\left\langle \int_{-\infty}^{+\infty} dv_\parallel \int_0^{+\infty} dv_\perp \delta(\omega - n\omega_c - k_\parallel v_\parallel) F(\vartheta, v^i, v^j) \right\rangle . \tag{17}$$

The kernel is of the form

$$F(\vartheta, v^i, v^j) \propto v_\perp \frac{\partial g_{\rm sp}^\dagger}{\partial v^i} D_0^{ij} \frac{\partial f_M}{\partial v^j}, \tag{18}$$

where constant factors have been omitted. This kernel is integrated along the resonance line defined by the delta-function to obtain the driven current density. It should be noted that on the $(v_\perp, v_\parallel)$-plane the resonance lines are lines of constant parallel velocity in the non-relativistic case, circles in the weakly-relativistic approach, and elliptic curves in the fully relativistic approach whose centers are located at the $v_\perp = 0$ axis, respectively.

This paper extends the studies of Ref. 8, where the DKES code[27] is used for the computation of the ECCD efficiency with a simplified collision model for small but finite collisionalities. In contrast, NEO-2 is used here for the computation of the generalized Spitzer function without simplifications on device geometry or on the collision operator. In order to investigate finite collisionality effects on a broad range of launch angles, scans over the poloidal launch angle α (angle between the horizontal plane and the beam) and the toroidal launch angle β (angle between the beam and the meridian plane containing the launcher) are presented in the following for the X2- and the O2-scenario. The second harmonic extraordinary mode (X2) with oblique propagation, sufficient for significant ECCD, is usually characterized by almost total absorption before the beam reaches the position of cold resonance $\omega = n\omega_{c0}$, while the second harmonic ordinary mode (O2) has overall lower absorption (typically 50% to 80% for the first pass). However, weak absorption of the O2-mode allows deeper penetration into the plasma and therefore, a significant amount of power absorption by trapped particles. It is necessary to clarify that the investigated launch angles are of theoretical interest and capabilities of the mirrors and other device constraints where not taken into account. As a test configuration one beam with $P_{\rm inp} = 1$ MW input power and a frequency of 140 Ghz is launched off axis ($Z = 0.1$ m), from an origin given in cylindrical coordinates of $R = 6.56$ m and $\varphi = -6.5$ deg. This position is close to the bean-shaped plane.

1. Low and moderate density scenario - X2-mode

The common Wendelstein 7-X scenario for low and moderate plasma densities ($n_e < 1.2 \cdot 10^{14}$ cm^{-3} for 140 GHz and 2.5 T) for heating and current drive is the X2-scenario. The restriction on moderate densities origins from the plasma wave cut-off. As seen from the total power absorption in Fig. 7 (upper plane) for various launch angles, the X2-mode is characterized by total absorption for launch angles where the resonance condition can be fulfilled. The optical thickness of the plasma for the X2-wave results in power absorption mainly by passing particles before the cold resonance position is reached. However, as shown in Ref. 8, finite collisionality leads to an offset in the antisymmetric passing part of the distribution function, which can influence current drive also for scenarii, where no wave energy is absorbed by trapped particles. In Fig. 7 (lower plane) the total parallel current driven by passing and trapped particles is depicted. The sign of this current is mainly determined by the parallel wave number $k_\parallel$, thus strongly depends on the toroidal launch angle. Two particular launch angles are investigated in more detail, namely ($\alpha = 5$ deg, $\beta = 20$ deg) and ($\alpha = 18.75$ deg, $\beta = -2.5$ deg), which are in the following referred to as X2a and X2b, respectively.

Scenario X2a (Fig. 8) is characterized by total absorption of the wave energy by strongly passing particles before the beam reaches the position of cold resonance. However, compared to the collisionless model, a visible increase of the current due to an offset to the antisymmetric part of the generalized Spitzer function is observed. In Fig. 9 the integral kernel (18) of the generated current density is plotted in the $(v_\perp, v_\parallel)$-plane for the finite collisionality and the collisionless model with three resonance lines corresponding to positions along the central ray path shown in Fig. 8. In this qualitative dependence, in contrast to Fig. 8, beam attenuation along its path caused by the absorption is ignored in F, where the wave amplitude has been set constant everywhere for simplicity. It should be noted that the integral kernel F depends on the spatial position, therefore it is different for different resonance positions, however, the change is minimal within the three depicted resonance positions and not of relevance for this qualitative view. As can be seen from Fig. 8, the strong absorption of the X2-mode does not allow any power absorption by trapped particles, which is usually expected for X2-scenarii. In Fig. 10, where the total driven current within the volume enclosed by a given flux surface is plotted, it can be seen that the collisionless model

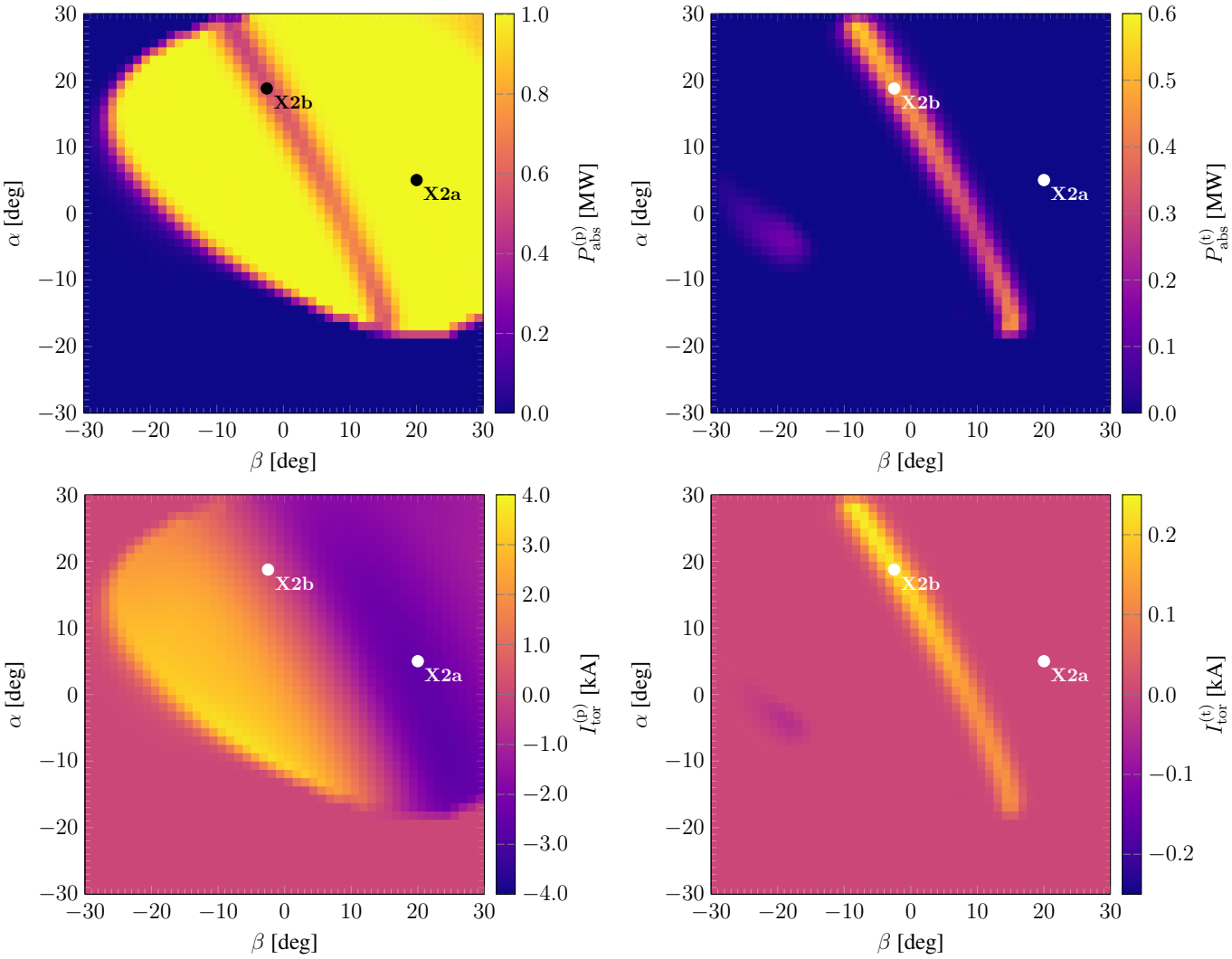

FIG. 7. X2-mode - Total absorbed power (upper plane) and total driven current (lower plane) of a beam with 1 MW input power as functions of the toroidal (β) and poloidal (α) launch angle by passing particles (left) and trapped particles (right). Two particular launch angles, depicted as X2a and X2b, are then studied in more detail.

underestimates the total current by approximately 10%.

Scenario X2b (Fig. 11), which is characterized by very low $k_{\parallel}$, is special for X2 since almost the same fraction of energy is absorbed by trapped and passing particles in a very narrow absorption region (roughly 1 cm) after the cold resonance position. As a consequence, a current is driven by both, trapped and passing particles, which is significantly underestimated by the collisionless model. Again, in Fig. 12 the integral kernel (18) of the parallel current density is depicted for the finite and collisionless model. As can be seen, a

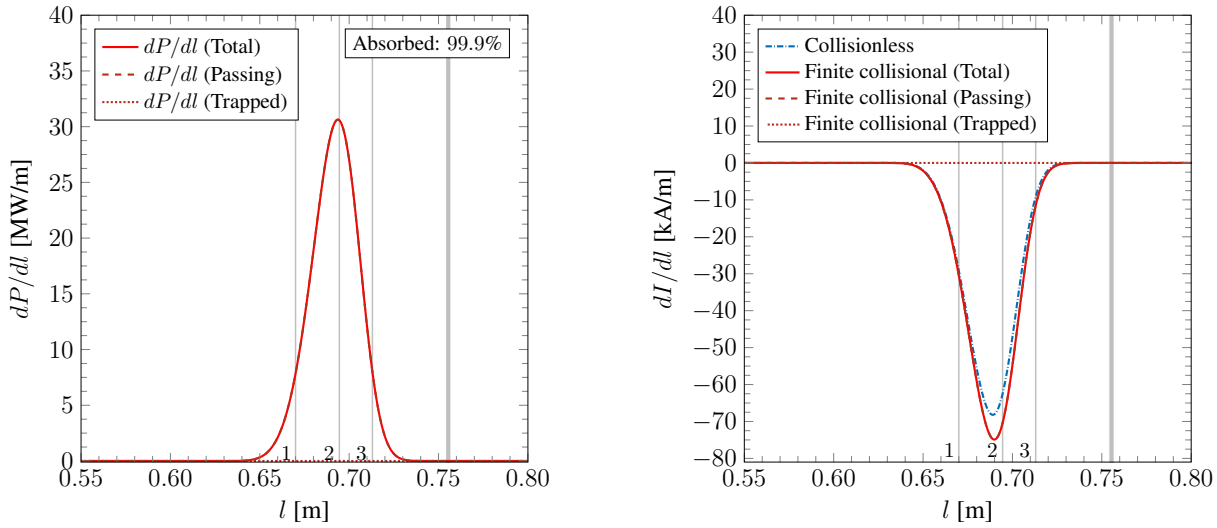

FIG. 8. Scenario X2a - Locally absorbed power dP/dl (left) and locally driven current dI/dl (right) for the finite collisionality and the collisionless case as functions of the distance along the central ray l. Contributions of passing and trapped particles are depicted as dashed and dotted lines, respectively. The cold resonance position is marked with a thick vertical line.

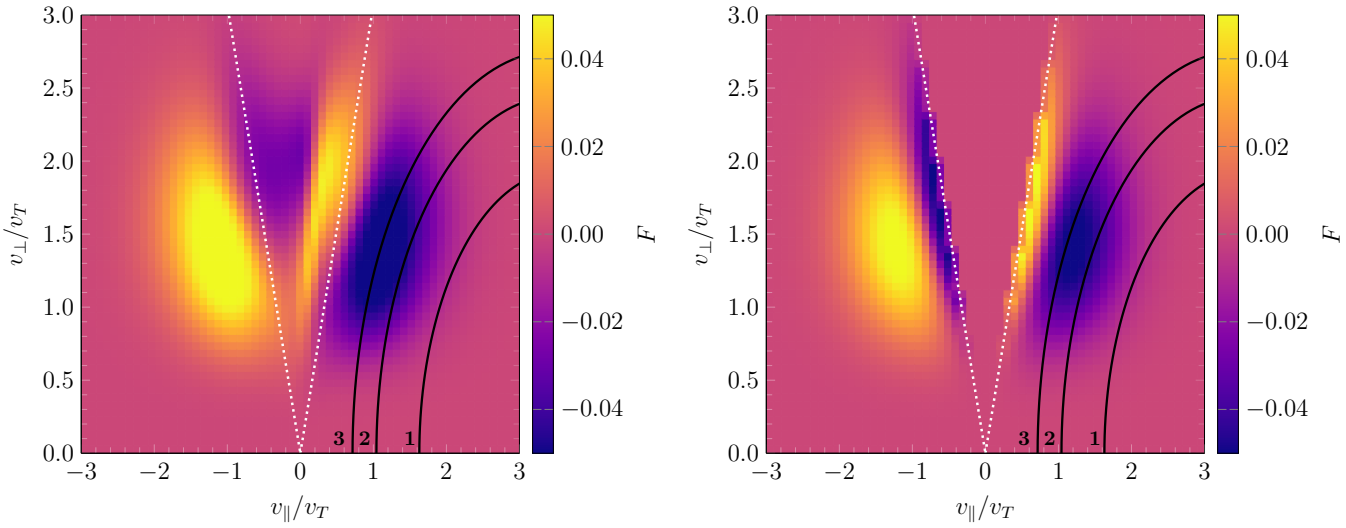

FIG. 9. Scenario X2a - Current density integral kernel (18) as a function of the parallel and perpendicular normalized velocities for finite collisionality (left) and for the collisionless limit (right). The three numbered resonance lines correspond to respective positions indicated by numbered vertical lines in Fig. 8. The trapped-passing boundary is shown by dashed lines. Colors are supersaturated in order to clarify the different signs of kernel F in different regions.

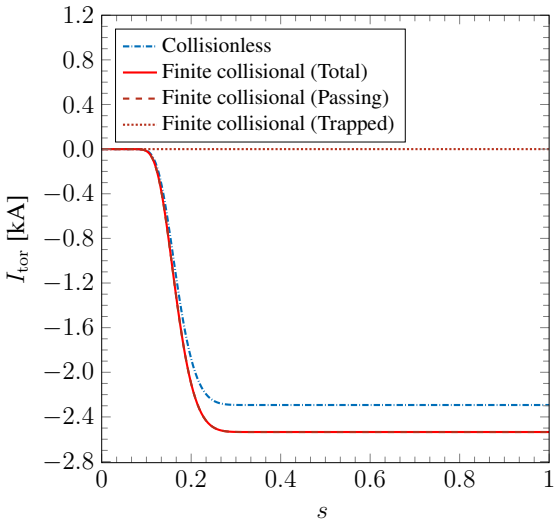

FIG. 10. Scenario X2a - Total driven current within the volume enclosed by a given flux surface s for finite collisionality and in the mean free path regime.

significant fraction of resonance line 2 is located inside the deeply trapped region. In contrast to the collisionless model where the distribution function is strictly antisymmetric and the integral kernel vanishes in the trapped domain, this significantly increases the integral along the resonance line leading to a co-current by trapped particles. In Fig. 13 the total driven parallel current indicates that account of finite plasma collisionality for this particular launch angle leads to an increase of the total current by almost one order of magnitude. This current increase mainly results from a non-vanishing symmetric part of the generalized Spitzer function in the trapped domain referred to as the "Helander-Catto-effect"[10].

In addition, an angle scan over the toroidal angle β at a fixed poloidal launch angle $\alpha = 18.75$ deg is given in Fig. 14. As can be seen, for small toroidal launch angles, a significant amount of energy is absorbed by trapped particles, resulting in a current which is clearly underestimated by the collisionless model.

2. High density scenario - O2-mode

In contrast to the X2-mode, the plasma is optically gray for the O2-mode, thus the energy of the wave is not fully absorbed within a single pass. The cut-off density is twice the cut-off density of X2, which makes the O2-scenario applicable for high-density plasmas. 2D launch angle scans in Fig. 15, similar to scans of Fig. 7 for X2, show that the sign of the total driven

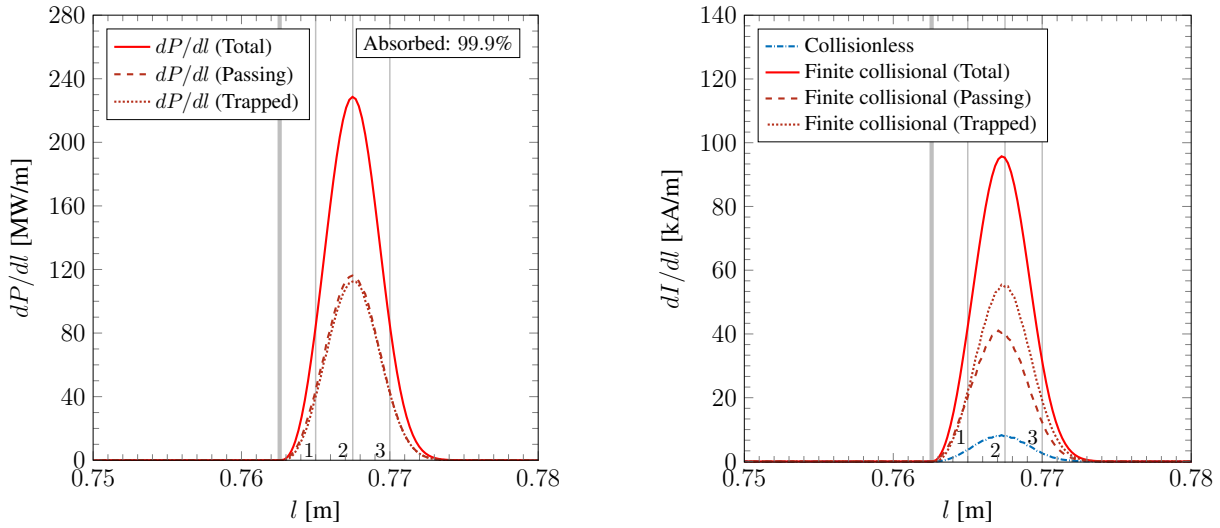

FIG. 11. The same as in Fig. 8 for scenario X2b.

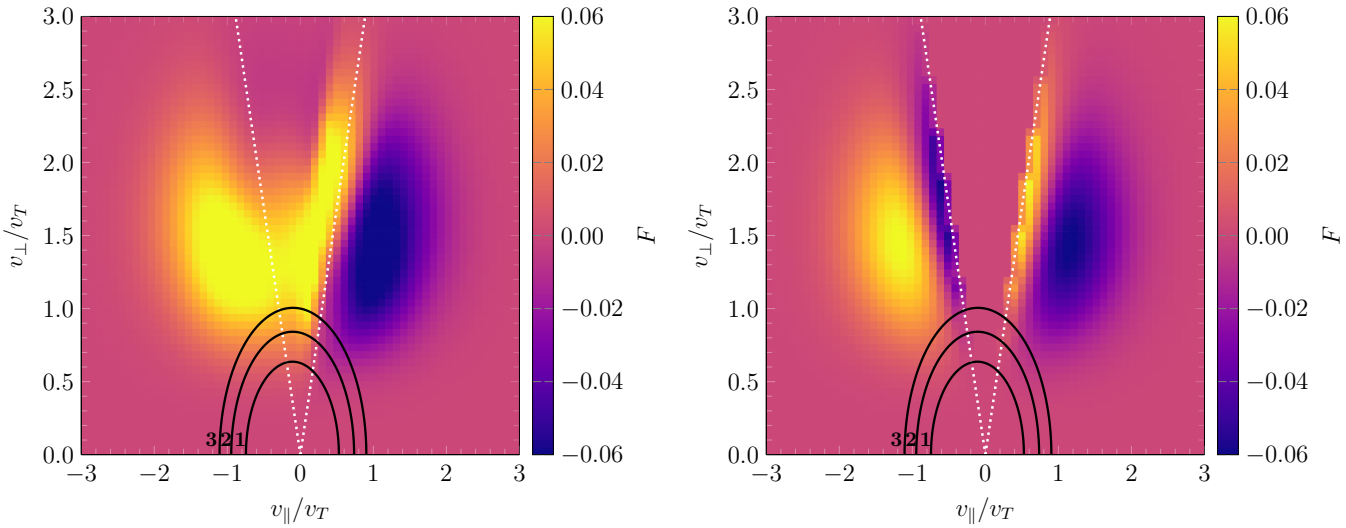

FIG. 12. The same as in Fig. 9 for scenario X2b. The three numbered resonance lines correspond to respective positions indicated by numbered vertical lines in Fig. 11.

current by passing particles is mainly determined by the toroidal launch angle which mainly determines the parallel wave number $k_\parallel$. However, the sign of the total current driven by trapped particles is mainly determined by the poloidal position of absorption region. This is in agreement with the behavior of the pitch-angle integral of the generalized Spitzer function in the trapped domain (13) in Fig. 6. Also for the O2-scenario two particular launch angles are investigated, namely ($\alpha = 5$ deg, $\beta = 20$ deg), which is the same as X2a, and ($\alpha = 0$ deg, $\beta = -10$ deg), which are in the following referred to as O2a and O2b, respectively.

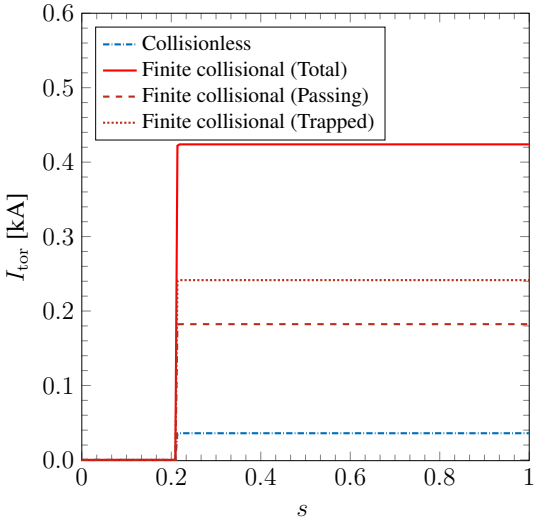

FIG. 13. The same as in Fig. 10 for scenario X2b.

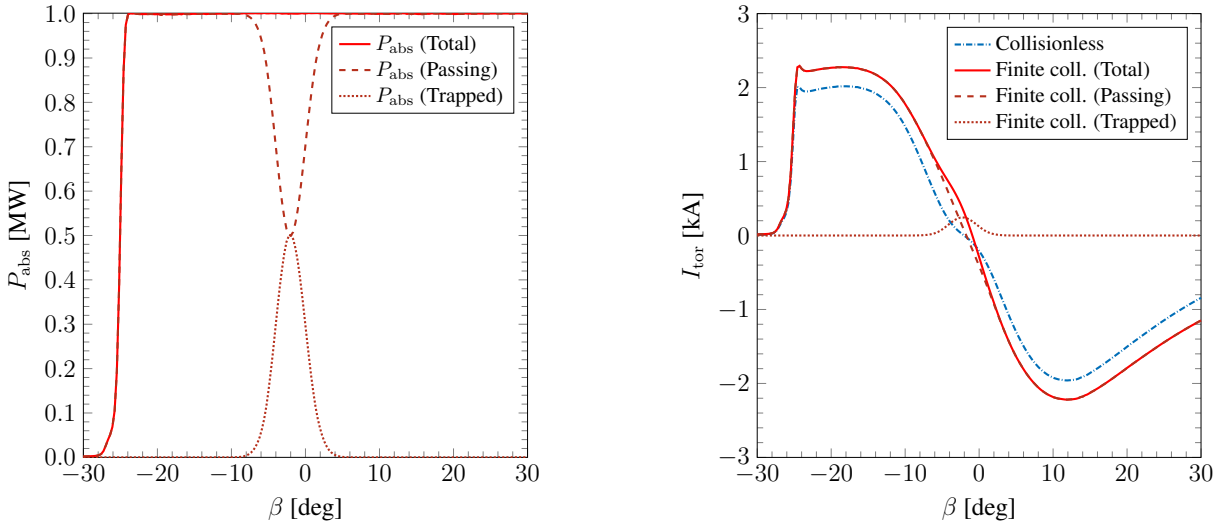

FIG. 14. Absorbed power (left) and total driven current (right) of a X2-beam with 1 MW input power by passing (dashed) and trapped (dotted) particles as a function of the toroidal launch angle β at fixed poloidal angle $\alpha = 18.75$ deg.

In launch scenario O2a (Fig. 16) a major fraction of energy is absorbed by passing particles before the cold resonance surface, and a significant amount is also absorbed by trapped particles after the cold resonance surface. The resonant parallel velocity changes its sign after the cold resonance position, thus leading to both, co- and counter-current by passing particles at different sides of cold resonance, respectively. However, the significant amount of trapped particles involved in the absorption process leads to a pertinent current in

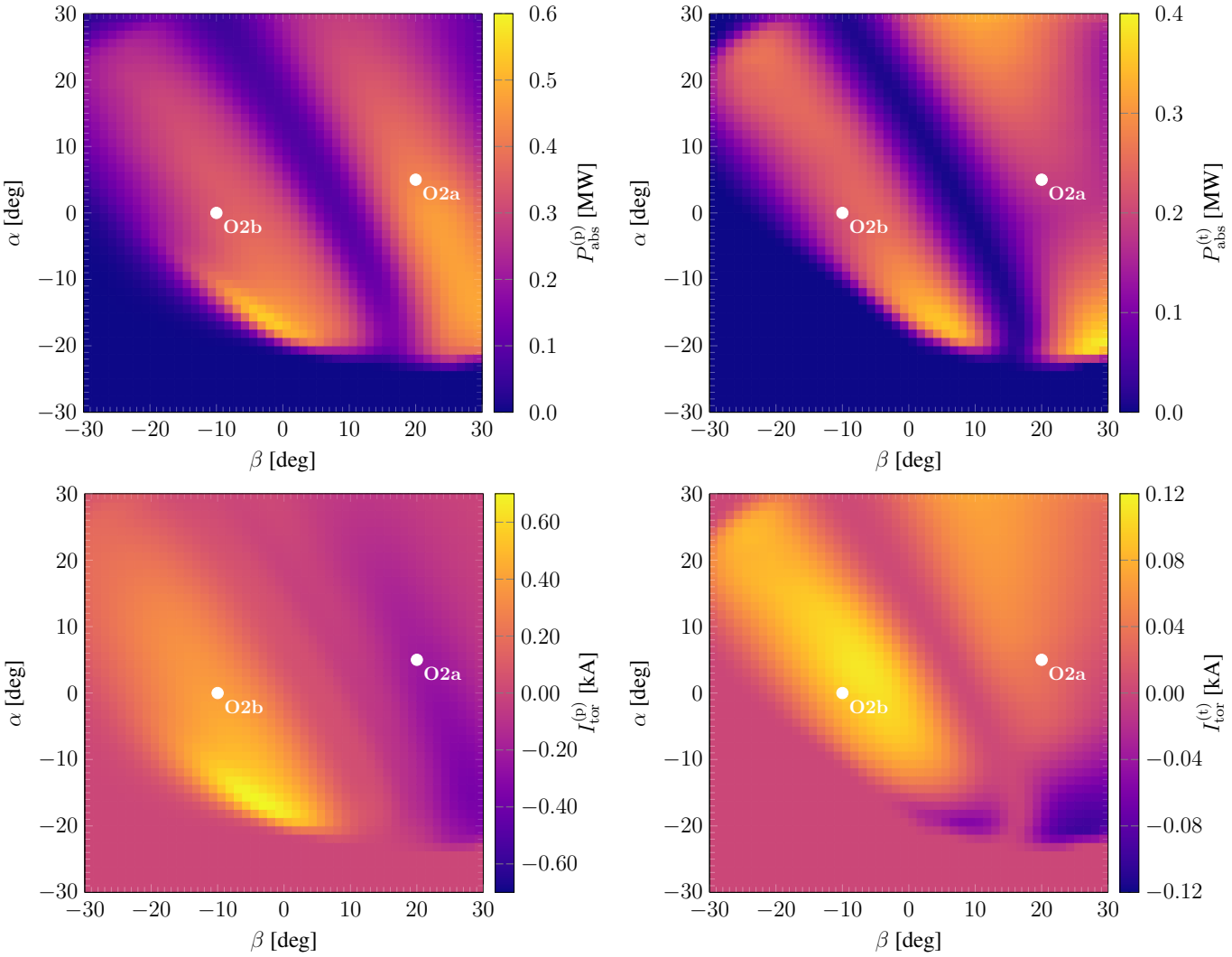

FIG. 15. The same as in Fig. 7 for the O2-resonance. Two particular launch angles, depicted as O2a and O2b, are then studied in more detail.

contrast to the collisionless model. For detailed investigation of the different current drive mechanisms, the integral kernel (18) of the current density in Fig. 17 is presented. The resonance line at position 1 is fully located in the passing region, what results in a counter-current drive by passing particles only. Integration along resonance line 2 covers both, passing and trapped region. Here, a co-current is generated by a non-vanishing symmetric part of the generalized Spitzer function in the trapped domain. The resonance line at position 3 is almost fully in the passing domain, which results in a co-current by passing particles and almost no contribution from trapped particles. As can be seen in Fig. 18, the increase of the total driven current by passing particles is mitigated by the different sign

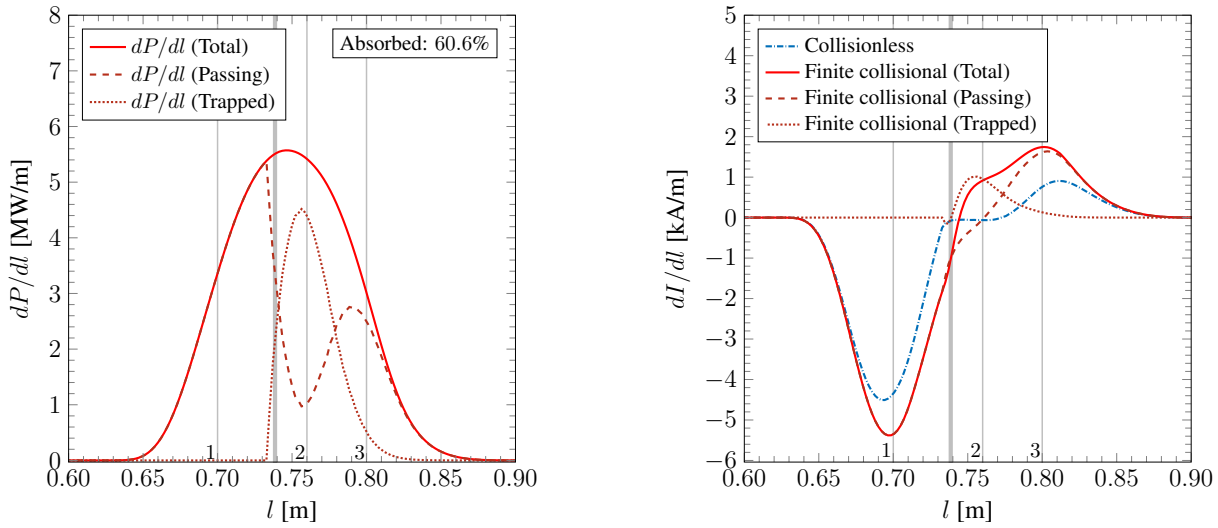

FIG. 16. The same as in Fig. 8 for scenario O2a.

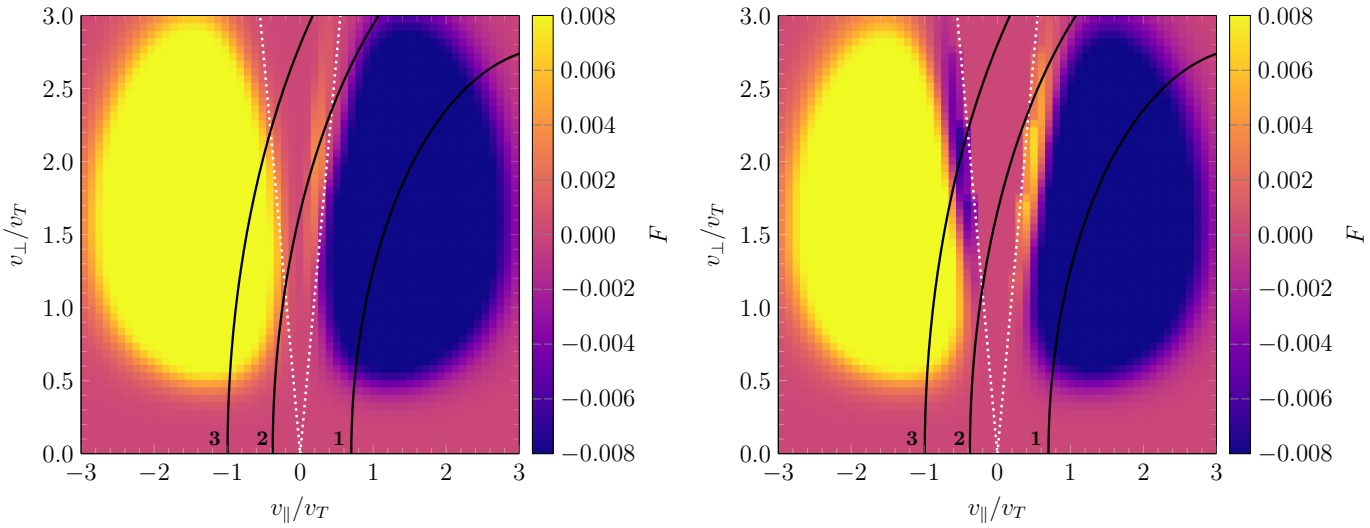

FIG. 17. The same as in Fig. 9 for scenario O2a. The three numbered resonance lines correspond to respective positions indicated by numbered vertical lines in Fig. 16.

of the current by trapped particles. In order to maximize the current drive, a scenario has to be found where both, current driven by trapped and passing particles, have the same sign and where absorption processes prohibits damping of the current due to the change of the sign of the resonant parallel velocity when passing the cold resonance position. Such a launch angle scenario has been found and is presented in the following.

In scenario O2b (Fig. 19) the current by trapped particles significantly increases the total driven current since the counter-current by passing particles is not strong enough to mitigate

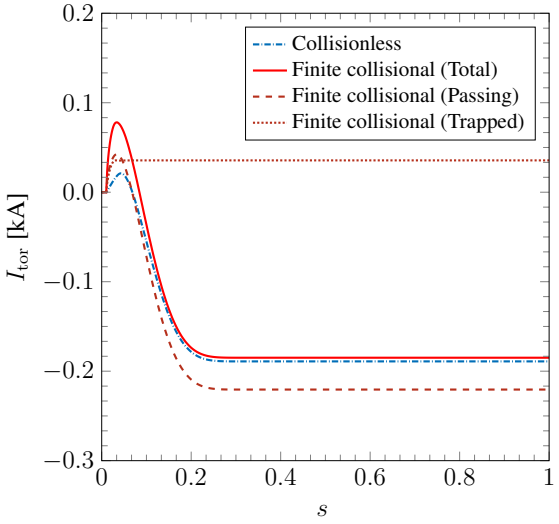

FIG. 18. The same as in Fig. 10 for scenario O2a.

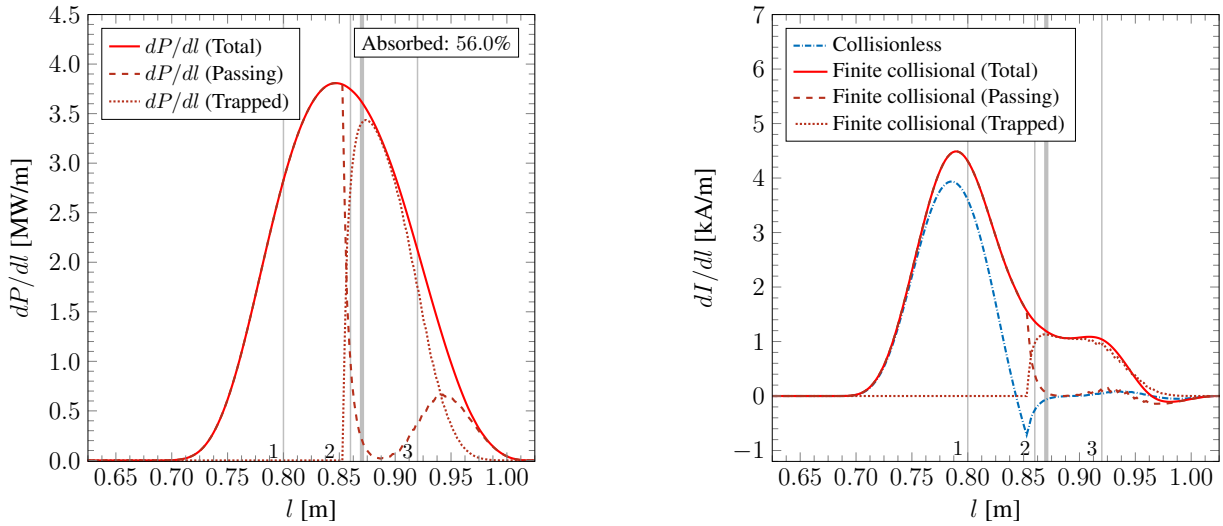

FIG. 19. The same as in Fig. 8 for scenario O2b.

this effect. In Fig. 20, where the current density kernel (18) is plotted, it is clearly seen that at resonance position 1 the whole current is produced by passing particles, while in contrast to the collisionless model, at positions 2 and 3 there is a non-vanishing contribution to the generated current in the trapped domain close to the boundary layer. As seen from the total driven current in Fig. 21, the collisionless model underestimates the current by 60%.

Out of all figures, Fig. 19 is the best to illustrate all three current drive mechanisms involved, which do not require momentum input. First, and the strongest of them, is the Fish-Boozer mechanism[3] which results from the dependence of momentum relaxation time

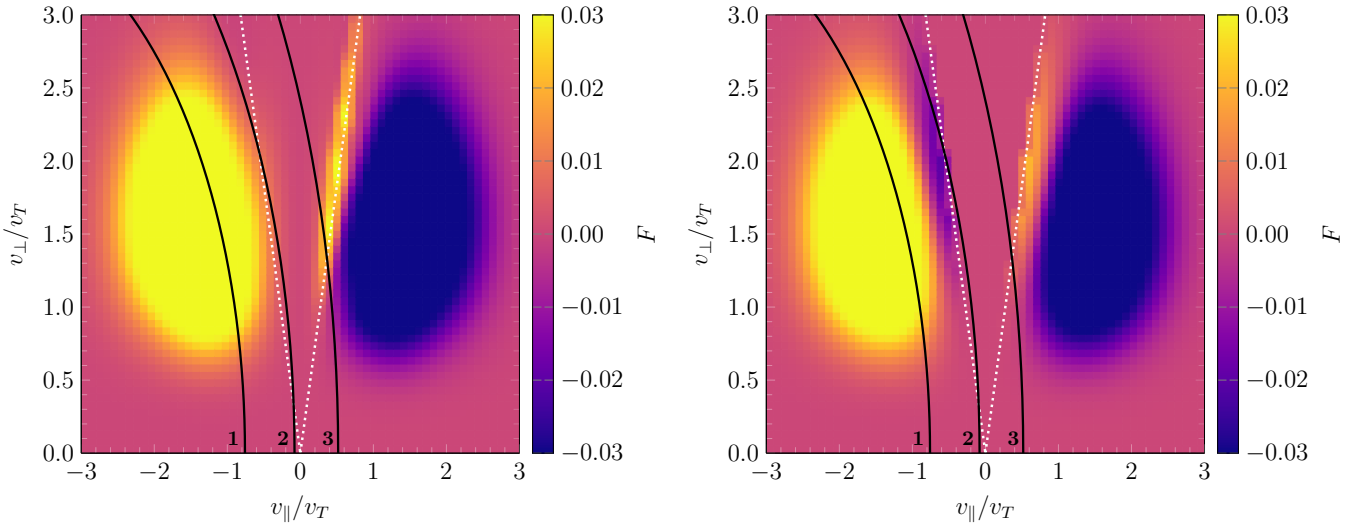

FIG. 20. The same as in Fig. 9 for scenario O2b. The three numbered resonance lines correspond to respective positions indicated by numbered vertical lines in Fig. 19.

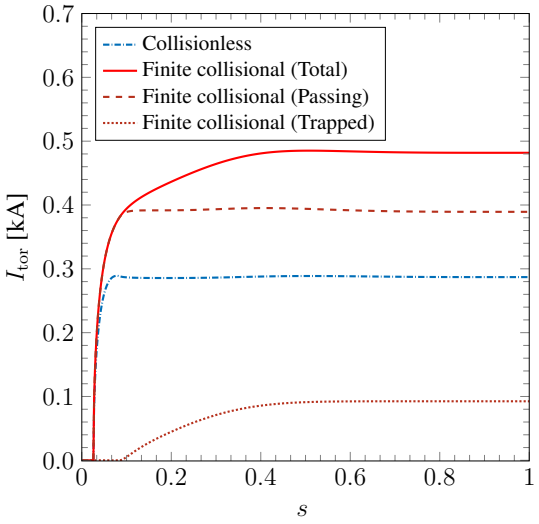

FIG. 21. The same as in Fig. 10 for scenario O2b.

on the position in the velocity space due to such a dependence of the local collision time. This mechanism prevails in velocity space regions where F is negative for $v_\parallel > 0$ and, respectively, positive for $v_\parallel < 0$ (F is with high accuracy antisymmetric there). Another mechanism can be called a "collisional Ohkawa effect", called also a "trapped particle effect" in Ref. 28. This mechanism also follows from the momentum relaxation time dependence on the velocity which is induced now by the proximity of the trapped particle region ("momentum loss cone"). The region where this mechanism prevails can be seen in the collisionless figure,

Fig. 19 (right), near the trapped-passing boundary in the passing particle domain. There, the sign of F changes to the opposite with respect to the sign of F in the regions with Fish-Boozer mechanism. It should be noted that the term "collisional Ohkawa effect" is used here in order to distinguish from the conventional Ohkawa effect[29], where the current is generated by rf-diffusion alone which enforces the particle exchange between trapped and passing regions. In turn, the "collisional Ohkawa effect" does not require the capability from the rf-diffusion to move particles into the loss cone directly. It is sufficient for this diffusion just to move particles closer to the trapped-passing boundary and the rest is completed by collisions. Finally, in addition to these two mechanisms which are basically described by the antisymmetric part of the generalized Spitzer function, also the "Helander-Catto mechanism" can be seen in the collisional figure, Fig. 19 (left), where the symmetric part of F makes a contribution in the trapped particle domain and in the vicinity of the trapped-passing boundary in the passing region.

IV. CONCLUSION

It has been shown that finite collisionality effects have an impact on the total current driven in both, ECCD scenarii where the wave energy is fully absorbed by passing particles and in scenarii where also trapped particles are involved in the absorption process. For proper description of these effects the generalized Spitzer function was computed by the drift kinetic equation solver NEO-2 for a high-mirror configuration of Wendelstein 7-X using realistic plasma parameters representing an initial stage of device operation without simplifications on the collisional model. This 5D function is used in the ray-tracing code TRAVIS and extends its various collisionless models. From the NEO-2 results it is seen that the generalized Spitzer function exhibits symmetric parts, which are responsible for current drive by waves with symmetric spectra[10], which can not be expected from interpolation between asymptotical collisionality limits. The impact of finite collisionality is not only restricted to the trapped domain but also leads to an offset of the generalized Spitzer function in the passing domain and therefore to an increase of its antisymmetric part. This is investigated in more detail in Ref. 8. However, the significance of these finite collisionality effects decreases at higher particle velocities and lower collisionality, respectively. While the strong absorption of the X2-scenario for low and moderate densities results in efficient cur-

rent generation, in high density plasmas this mode can not propagate through the plasma because of the wave cut-off. For such scenarii heating and current drive with the O2-mode might become necessary. Since the overall low absorption of the O2-mode, also multi-pass scenarii are planed, while in this paper only the first pass was investigated.

It has also been demonstrated that the precomputation not only is possible for flux surface averaged quantities such as diffusion coefficients, but also for the high dimensional distribution function. Various techniques such as usage of the HDF5 data storage format and data caching capabilities of the provided data interface, allow straightforward and fast access to the data. The precomputation would not be possible within reasonable effort without the efficient parallelization of the code NEO-2.

The ray-tracing code TRAVIS uses a fully relativistic approach for the computation of the resonance condition and the absorption and emission coefficients. Up to now, NEO-2 models the generalized Spitzer function in the non-relativistic limit (for the applied plasma parameters, this does not produce any significant error in ECCD calculations). However, this is not a limitation of the code itself and can be generalized using a collision operator treating relativistic effects. This is a pending task for the nearest future.

ACKNOWLEDGMENTS

This work has been carried out within the framework of the EUROfusion Consortium and has received funding from the Euratom research and training programme 2014-2018 under grant agreement No 633053. The views and opinions expressed herein do not necessarily reflect those of the European Commission. The authors gratefully acknowledge support from NAWI Graz and funding from the OeAD under the grant agreement "Wissenschaftlich-Technische Zusammenarbeit mit der Ukraine" No UA 06/2015. The computational results presented have been achieved in part using the Vienna Scientific Cluster (VSC).

REFERENCES

[1]G. Grieger, W. Lotz, P. Merkel, J. Nührenberg, J. Sapper, E. Strumberger, H. Wobig, R. Burhenn, V. Erckmann, U. Gasparino, L. Giannone, H. J. Hartfuss, R. Jaenicke,

G. Kühner, H. Ringler, A. Weller, F. Wagner, the W7X Team, and the W7AS Team, Physics of Fluids B **4**, 2081 (1992).

[2]M. Romé, V. Erckmann, U. Gasparino, and N. Karulin, Plasma Physics and Controlled Fusion **40**, 511 (1998).

[3]N. J. Fisch and A. H. Boozer, Phys. Rev. Lett. **45**, 720 (1980).

[4]V. Erckmann, P. Brand, H. Braune, G. Dammertz, G. Gantenbein, W. Kasparek, H. P. Laqua, H. Maassberg, N. B. Marushchenko, G. Michel, *et al.*, Fusion Science and Technology **52**, 291 (2007).

[5]T. M. Antonsen and K. R. Chu, Physics of Fluids **25**, 1295 (1982).

[6]L. Spitzer Jr and R. Härm, Physical Review **89**, 977 (1953).

[7]Y. R. Lin-Liu, V. S. Chan, F. L. Hinton, and S. K. Wong, AIP Conference Proceedings **595**, 438 (2001).

[8]H. Maaßberg, C. D. Beidler, and N. B. Marushchenko, Physics of Plasmas **19**, 102501 (2012).

[9]Y. R. Lin-Liu, V. S. Chan, T. C. Luce, R. Prater, O. Sauter, and R. W. Harvey, AIP Conference Proceedings **485**, 249 (1999).

[10]P. Helander and P. J. Catto, Physics of Plasmas **8**, 1988 (2001).

[11]W. Kernbichler, S. V. Kasilov, G. O. Leitold, V. V. Nemov, and N. B. Marushchenko, Contributions to Plasma Physics **50**, 761 (2010).

[12]W. Kernbichler, G. Kapper, S. V. Kasilov, and N. B. Marushchenko, in *EPJ Web of Conferences*, Vol. 87 (EDP Sciences, 2015) p. 01006.

[13]G. Kapper, W. Kernbichler, S. V. Kasilov, and N. B. Marushchenko, in *42nd EPS Conference on Plasma Physics* (European Physical Society, 2015).

[14]W. Kernbichler, S. V. Kasilov, G. Kapper, A. F. Martitsch, V. V. Nemov, C. Albert, and M. F. Heyn, Plasma Physics and Controlled Fusion (2016).

[15]V. V. Nemov, S. V. Kasilov, W. Kernbichler, and M. F. Heyn, Physics of Plasmas **6**, 4622 (1999).

[16]W. Kernbichler, S. V. Kasilov, G. O. Leitold, V. V. Nemov, and K. Allmaier, Plasma and Fusion Research **3**, S1061 (2008).

[17]C. Beidler, K. Allmaier, M. Isaev, S. Kasilov, W. Kernbichler, G. Leitold, H. Maaßberg, D. Mikkelsen, S. Murakami, M. Schmidt, D. Spong, V. Tribaldos, and A. Wakasa, Nuclear Fusion **51**, 076001 (2011).

[18]A. F. Martitsch, S. V. Kasilov, W. Kernbichler, G. Kapper, C. G. Albert, M. F. Heyn, H. M. Smith, E. Strumberger, S. Fietz, W. Suttrop, M. Landreman, The ASDEX Upgrade Team, and the EUROfusion MST1 Team, Plasma Physics and Controlled Fusion **58**, 074007 (2016).

[19]N. B. Marushchenko, Y. Turkin, and H. Maassberg, Computer Physics Communications **185**, 165 (2014).

[20]S. I. Braginskii, Reviews of plasma physics **1**, 205 (1965).

[21]C. de Boor, Journal of Approximation Theory **6**, 50 (1972).

[22]The HDF Group, (1997-2016), http://www.hdfgroup.org/HDF5/.

[23]Y. Turkin, C. D. Beidler, H. Maaßberg, S. Murakami, V. Tribaldos, and A. Wakasa, Physics of Plasmas **18**, 022505 (2011).

[24]S. P. Hirshman and J. C. Whitson, Physics of Fluids **26**, 3553 (1983).

[25]S. V. Kasilov and W. Kernbichler, Physics of Plasmas **3**, 4115 (1996).

[26]N. B. Marushchenko, C. D. Beidler, S. V. Kasilov, W. Kernbichler, H. Maaßberg, R. Prater, and R. W. Harvey, Physics of Plasmas **18**, 032501 (2011).

[27]S. P. Hirshman, K. C. Shaing, W. I. van Rij, C. O. Beasley, and E. C. Crume, Physics of Fluids (1958-1988) **29**, 2951 (1986).

[28]R. H. Cohen, Physics of Fluids **30**, 2442 (1987).

[29]T. Ohkawa, General Atomics Report GA-A13847 (1976).